# Effects of Crimped Fiber Paths on Mixed-Mode Delamination Behaviors in Woven Fabric Composites

**Paul V. Cavallaro**
**Andrew W. Hulton**
**NUWC Division Newport**

**Melvin W. Jee**
**U.S. Army Natick Soldier Research, Development & Engineering Center**

**Mahmoud Salama**
**JPS Composite Materials Corporation**

NAVSEA
WARFARE CENTERS
NEWPORT

# Naval Undersea Warfare Center Division Newport, Rhode Island

# PREFACE

**Reviewed and Approved: 1 September 2016**

*Eric S S pigel*

**Eric S. Spigel**
**Head, Ranges, Engineering, and Analysis Department**

# REPORT DOCUMENTATION PAGE

*Form Approved*
*OMB No. 0704-0188*

The public reporting burden for this collection of information is estimated to average 1 hour per response, including the time for reviewing instructions, searching existing data sources, gathering and maintaining the data needed, and completing and reviewing the collection of information. Send comments regarding this burden estimate or any other aspect of this collection of information, including suggestions for reducing this burden, to Department of Defense, Washington Headquarters Services, Directorate for Information Operations and Reports (0704-0188), 1215 Jefferson Davis Highway, Suite 1204, Arlington, VA 22202-4302. Respondents should be aware that notwithstanding any other provision of law, no person shall be subject to any penalty for failing to comply with a collection of information if it does not display a currently valid OPM control number.
**PLEASE DO NOT RETURN YOUR FORM TO THE ABOVE ADDRESS.**

| 1. REPORT DATE (DD-MM-YY) 01-09-2016 | 2. REPORT TYPE Technical Report | 3. DATES COVERED (From – To) |
|---|---|---|

**4. TITLE AND SUBTITLE**

Effects of Crimped Fiber Paths on Mixed-Mode Delamination Behaviors in Woven Fabric Composites

**5a. CONTRACT NUMBER**

**5b. GRANT NUMBER**

**5c. PROGRAM ELEMENT NUMBER**

**6. AUTHOR(S)**

Paul V. Cavallaro
Andrew W. Hulton
Melvin W. Jee
Mahmoud Salama

**5.d PROJECT NUMBER**

**5e. TASK NUMBER**

**5f. WORK UNIT NUMBER**

**7. PERFORMING ORGANIZATION NAME(S) AND ADDRESS(ES)**

Naval Undersea Warfare Center Division
1176 Howell Street
Newport, RI 02841-1708

**8. PERFORMING ORGANIZATION REPORT NUMBER**

TR 12,216

**9. SPONSORING/MONITORING AGENCY NAME(S) AND ADDRESS(ES)**

Naval Undersea Warfare Center Division
1176 Howell Street
Newport, RI 02841-1708

**10. SPONSORING/MONITOR'S ACRONYM**

NUWC

**11. SPONSORING/MONITORING REPORT NUMBER**

**12. DISTRIBUTION/AVAILABILITY STATEMENT**

Approved for public release; distribution is unlimited.

**13. SUPPLEMENTARY NOTES**

**14. ABSTRACT**

This research investigated the fracture toughness and crack propagation behaviors of woven fabric polymer composite laminates subjected to single- and mixed-mode loadings using numerical models. The objectives were to characterize the fracture behaviors and toughness properties at the fiber/matrix interfaces and to identify mechanisms that can be exploited for increasing delamination resistance. The mode I and mode II strain energy release rates $G_I$ and $G_{II}$, the effective critical strain energy release rate $G_{c\_eff}$, and crack growth stabilities were determined as functions of crimped fiber paths using mesoscale, two-dimensional multi-continuum finite-element models. Three variations of a plain-woven fabric architecture—each of which had different crimped fiber paths—were considered. The presence of mixed strain energy release rates at the mesoscale due to the curvilinear fiber paths was shown to influence the interlaminar fracture toughness and was explored for pure single-mode and mixed-mode global loadings. It was concluded that woven fabric composites provided a fracture toughness conversion mechanism (FTCM) and their toughness properties were dependent on and varied with position along the crimped fiber paths. The FTCM was identified as an advanced tailoring mechanism that can be further utilized to improve toughness and damage-tolerance thresholds especially when the mode II fracture toughness $G_{IIc}$ is greater than the mode I fracture toughness $G_{Ic}$.

**15. SUBJECT TERMS**

Crack Growth Stability    Crimp    Delamination    Fiber-Reinforced Composites    Finite-Element Analysis    Fracture Mechanics

Fracture Toughness    Mixed Modes    Strain Energy Release Rate

| 16. SECURITY CLASSIFICATION OF: | | | 17. LIMITATION OF ABSTRACT | 18. NUMBER OF PAGES | 19a. NAME OF RESPONSIBLE PERSON Paul V. Cavallaro |
|---|---|---|---|---|---|
| a. REPORT Unclassified | b. ABSTRACT Unclassified | c. THIS PAGE Unclassified | SAR | 31 | 19b. TELEPHONE NUMBER (Include area code) 401-832-5082 |

NSN 7540-01-280-5500

Standard Form 298 (Rev. 2-89)
Prescribed by ANSI Std. Z39-18
298-102

# TABLE OF CONTENTS

**Page**

# LIST OF ILLUSTRATIONS

**Figure**                                                                       **Page**

i

**LIST OF TABLES**

# LIST OF ABBREVIATIONS AND ACRONYMS

| | |
|---|---|
| 2-D | Two-dimensional |
| 3-D | Three-dimensional |
| $a_o$ | Initial debond length |
| ASTM | American Society for Testing and Materials |
| BK | Benzeggagh-Kenane |
| CZM | Cohesive Zone Model |
| DBT | Debond time |
| DCB | Double cantilever beam |
| $E$ | Elastic modulus |
| ELS | End-loaded split |
| FRP | Fiber-reinforced polymer |
| FB | Fully balanced laminate |
| FEA | Finite-element analysis |
| FTCM | Fracture toughness conversion mechanism |
| $G$ | Shear modulus |
| $G_I$, $G_{II}$, $G_{III}$ | Mode-specific strain energy release rates |
| $G_{Ic}$, $G_{IIc}$, $G_{IIIc}$ | Mode-specific critical strain energy release rates |
| $G_{total}$ | Sum of $G_I$, $G_{II}$, $G_{III}$ |
| $G_{c\_eff}$ | Effective mixed-mode critical strain energy release rate |
| K | Kelvin |
| $L$ | Laminate length |
| LEFM | Linear elastic fracture mechanics |
| MMB | Mixed mode bending |
| $r$ | Radial distance from crack tip |
| SB | Semi-balanced laminate |
| $S_{LX}$, $S_{LY}$, $S_{LXY}$ | Transformed stress components along local fiber path coordinate system |
| $S_X$, $S_Y$, $S_{XY}$ | Global stress components along fiber path |
| TSL | Traction Separation Law |
| UB | Unbalanced laminate |
| VCCT | Virtual Crack Closure Technique |
| WFRP | Woven fabric-reinforced polymer |
| XFEM | Extended finite-element method |
| $X$ | Distance from initial debond front |
| $\overleftarrow{X}$ | Applied force location on loading bar |
| $\eta$ | Material curve fit parameter for Benzeggagh-Kenane mixed-mode fracture criterion |
| $\lambda$ | Crimp wavelength |
| $\nu$ | Poisson's ratio |
| $\theta$ | Angle measured from the tangent vector along the fiber path to the global x-axis |

# EFFECTS OF CRIMPED FIBER PATHS ON MIXED-MODE DELAMINATION BEHAVIORS IN WOVEN FABRIC COMPOSITES

## INTRODUCTION

Woven fabric-reinforced polymer (WFRP) composites have become an important resource for structures that require lightweight materials and are capable of operating in and surviving against severe dynamic loading events such as blast, ballistic and fragment impacts, and mechanical shock. The applicability of WFRP composites to primary load-carrying structures, however, is often limited because of complexities involving localized mechanics that span across multiple material length scales. These complexities influence the failure thresholds and damage mechanisms in WFRP composites and are difficult to simulate in numerical models. Specifically, numerical simulations that employ homogenization techniques at the ply and laminate levels explicitly lack the critical details of the fiber paths and the fiber-matrix interfaces to address the influence of woven fabric architectures on fracture behaviors and interfacial delaminations.

The research documented in this report shows that these behaviors can be investigated through mesoscale multi-continuum models, the data from which can contribute to the identification of new and advanced tailoring methods to improve structural performance of composites by increasing fracture resistance, damage tolerance, and energy absorption capacities.

## PUBLISHED RESEARCH RELATED TO CHARACTERIZING FRACTURE TOUGHNESS AND CRACK PROPAGATION PROPERTIES

This section highlights salient developments in performance modeling for fracture toughness and crack propagation behaviors of fiber-reinforced polymer (FRP) composite laminates. A commonly used method to perform numerical modeling of mixed-mode crack growth in laminated composites is the virtual crack closure technique (VCCT), originally proposed by Rybicki and Kanninen.[1] The technique is based on linear elastic fracture mechanics (LEFM) and the principle that the energy released during crack extension is the energy required to close the crack. Krueger[2] provided in-depth descriptions of VCCT historical developments, detailed theoretical descriptions for its implementation in finite-element analysis (FEA) codes, and descriptive examples for multidimensional, bi-material interface applications. Unlike traditional stress-based approaches, which require locally refined crack-tip meshes and specialized quarter-point crack-tip elements to yield the $1 / \sqrt{r}$ singularity (where $r$ is the radial distance from crack tip), the VCCT provides an efficient alternative to numerical modeling of crack propagations by using a kinematic approach to structures containing an initial crack. Here the nodal forces, opening and sliding displacements, are tracked, and the mode-specific strain

energy release rates are computed and compared to fracture toughness properties of the material modeled. Crack growth occurs when the effective mixed-mode strain energy release rate exceeds the material's fracture toughness in accordance with a governing mixed-mode crack growth criterion. Additional considerations are described for geometric nonlinearities and mismatched element sizes between interface surfaces.

Benzeggagh and Kenane[3] conducted experimental tests and fractography on 6-mm-thick E-glass/epoxy composite laminates subjected to mode I double-cantilever beam (DCB), mode II end-loaded split (ELS), and mixed-mode (I and II) bending (MMB) loads in displacement control. Benzeggagh and Kenane[3] presented a semi-empirical criterion for describing the mixed-mode fracture toughness—known as the BK mixed-mode fracture toughness criterion. Fractography analysis using a scanning electron microscope identified the presence of different fracture surfaces resulting from the mode I, mode II, and mixed-mode loadings. Mode I loading produced cleavage fractures in the epoxy and along the epoxy/fiber interfaces. Mode II loading produced epoxy fractures with shear hackles oriented at 45° to the fiber paths. This orientation was coincident with the plane of maximum principal stress, thus confirming the dominance of in-plane shear stresses. The mixed-mode loading produced fracture surfaces with combined cleavage and shear hackle fractures; however, as the mode mixity increased with increasing mode II contributions, the quantity of shear hackles increased and cleavage fractures decreased.

Shindo et al.[4] investigated the mixed-mode fracture behaviors in woven glass/epoxy laminates at several temperatures: room temperature, liquid nitrogen temperature (77°K), and cryogenic temperature using liquid helium (4°K). Experiments were performed using the ASTM-D-6671-06 MMB test[5]; both analytical and three-dimensional (3-D) FEA approaches were used to obtain strain energy release rates. The experimental results showed that (1) unstable crack growth occurred at the 77°K and 4°K temperatures and (2) the total critical strain energy release rates at room temperature and at 4°K increased with increasing mixity from mode II contributions. The FEA model treated the woven laminate as a homogeneous, orthotropic material and used the VCCT and BK mixed-mode fracture criterion to govern crack propagation. Homogenization performed at the ply level and above—a commonly used approach for modeling WFRP composites—does not allow the direct representation of the crimped fiber paths; therefore, the effects of crimp on fracture toughness cannot be simulated.

Ranatunga[6] investigated delamination initiation and crack propagation behaviors in unidirectional carbon fiber/epoxy composite laminates using laminate-level, homogenized FEA models that employed the VCCT and cohesive zone modeling (CZM) methods. The models were representative of the DCB test for evaluating mode I fracture toughness. The DCB specimen was similar to the MMB specimen and included a film insert to provide the initial debond length. Parameters influencing solution convergence and runtimes, including mesh refinement, viscous and stabilization energies, penalty stiffness (for CZM), and time-step size, were investigated. As demonstrated, both the VCCT and CZM approach to delamination initiation and propagation modeling must carefully consider these parameters to obtain reliable solutions.

Camanho and Dávila[7] described the development and use of zero-thickness volumetric decohesion finite elements to simulate delamination initiation and crack growth in composite

laminates. Their approach was similar to that of the CZM. A quadratic softening law was proposed for mixed-mode loadings. Both single- and mixed-mode progressive delamination models were developed. Comparison of the model results and physical test data showed good agreement.

Motamedi and Milani[8] discussed fracture analysis methods for modeling delaminations in composite materials subjected to mixed-mode loadings. These methods included the VCCT, CZM, and extended finite-element methods (XFEMs) for evaluating nonlinear fracture problems.

Hulton and Cavallaro[9] investigated fracture of a thin-walled, carbon fiber/epoxy matrix cylinder subject to quasi-static diametral compression using experiments and XFEM modeling. The cylinder was constructed of unidirectional (non-woven) tapes oriented along the hoop and longitudinal axes. The XFEM model used ply-level homogenization. Crack initiation loads and crack growth behaviors were monitored. Comparison of experimental and XFEM results showed that the predicted primary fracture mode and crack initiation site matched those observed from testing. Fracture initiated via mode I behavior in the outer longitudinal ply propagated radially inward and deflected at an inner 90° ply; a mode I cohesive interface failure developed along the hoop direction. The study demonstrated the effectiveness of using XFEM to model fracture in fiber-reinforced composites without requiring prior knowledge of crack initiation and propagation paths.

Hawkins and Haque[10] performed experimental mode I tests on 10-ply unidirectional carbon/epoxy laminates with and without graphene nanoparticle reinforcements (0.1% by weight) using the DCB specimen in displacement-controlled loading. The mode I critical strain energy release rates ($G_{Ic}$) were measured and compared. It was concluded that the three-phase carbon/graphene/epoxy laminate provided an 8.3% increase in $G_{Ic}$ over the conventional carbon/epoxy laminates.

Cavallaro[11] experimentally investigated the effects of several fabric weave styles and crimp gradients on the damage tolerance and energy absorption capacities in 20-ply Kevlar/epoxy composite laminates. The experimental results demonstrated that weave styles and crimp gradients can be used to alter the spatial and temporal behaviors of stress wave propagations and can increase damage tolerance and energy absorption capacities for static and severe dynamic loading events.

This report documents the results of research that focused on the influence of the curvilinear fiber paths developed from weaving on the fracture toughness and crack propagation behaviors of the fiber/matrix interfaces by performing two-dimensional (2-D), multi-continuum FEA using VCCT with the BK mixed-mode fracture criterion. This research also explored the presence of any localized mixed-fracture modes produced at these interfaces as a result of single-mode global loadings. The presence of localized mixed modes can be leveraged as a mechanism for increasing the fracture toughness and reducing interfacial delaminations in WFRP composites. Unlike unidirectional polymer composites in which the fiber paths are straight, WFRP composites have increased damage tolerance, possibly resulting from localized mixed-mode fracture behaviors. The findings of this research will provide new and advanced methods for improving the structural performance of WFRP composites.

## MODEL DEVELOPMENT

Multi-continuum mesoscale models were developed using ABAQUS[12] FEA software to quantify the primary and secondary strain energy release rates that are present during pure mode I, mode II, and mixed-mode global loadings on delaminations of the fiber/matrix interfaces. Figure 1 illustrates the conventional fracture modes considered for this modeling effort. The component strain energy release rates were obtained using VCCT; the mixed-mode responses were resolved using the BK fracture criteria. The variations of localized mode I and mode II strain energy release rates were captured over a one-half crimp wavelength and compared. The numerical results provide confirmation that fracture behaviors are dependent on the crimped fiber paths and that mixed-mode fracture behaviors exist at the mesoscale for single- and mixed-mode global loadings.
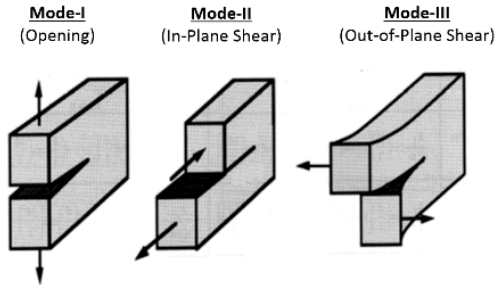


*Figure 1.  Fracture Modes*

Three laminate models were developed at the mesoscale with each laminate constructed of three plain-woven plies. The plies for each individual laminate were consistent; however, the three models contained different crimped fiber paths and were identified in terms of their warp and weft crimp distributions as fully balanced (FB), semi-balanced (SB) and unbalanced (UB) as shown in figure 2. The laminate models were loaded in a manner representative of the MMB test fixture.
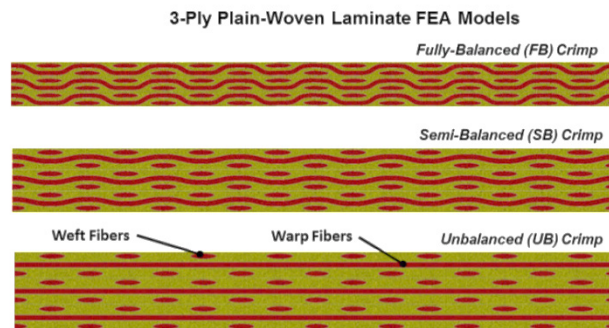


*Figure 2.  Three Laminate Models Constructed of Three-Ply Plain-Woven Fabrics with Different Crimped Fiber Paths*

The fiber and matrix materials were idealized as linearly elastic and isotropic using the properties listed in table 1. A more definitive representation of actual fibers modeled as homogenized yarn forms would suggest using a transversely isotropic behavior; however, sufficient material property data were not available to describe the fiber yarn forms. Cross sections of the weft fiber yarns were modeled as ellipsoidal. The separation distances between the warp and weft fibers were consistent across all three laminate models (see table 2 for additional model geometry details).

### Table 1.  Material Properties

| Material | $E$ (psi) | $v$ | $G$ (psi) |
|---|---|---|---|
| Fiber | $10.0 \times 10^6$ | 0.33 | $3.74 \times 10^6$ |
| Matrix | $1.0 \times 10^6$ | 0.27 | $3.94 \times 10^5$ |

### Table 2.  Model Geometry Details

| Parameter | Value |
|---|---|
| Model Length | 1.2512 in. |
| FB Laminate Thickness | 0.1080 in. |
| SB Laminate Thickness | 0.1347 in. |
| UB Laminate Thickness | 0.1620 in. |
| Warp Thickness | 0.0126 in. |
| Maximum Weft Thickness | 0.0126 in. |
| Maximum Weft Width | 0.0548 in. |
| Weft Width/Thickness Ratio | 4.3492 |
| Weft Density | 6.394 yarns/in. |
| One-Half Crimp Wavelength ($\lambda/2$) | 0.0780 in. |
| Initial Debond Length ($a_0$) | 0.1560 in. |

The MMB test fixture, initially designed by Reeder,[13] was represented in the model shown in figure 2 to apply the global mode I, global mode II, and global mixed-mode loadings (modes I and II). Note that this fixture and the 2-D models do not support mode III loadings.

The degree of mode mixity was controlled by varying the location of the applied force as shown in figure 3. The force was applied to the loading bar at a constant rate with respect to time. This type of loading is referred to as "force-control loading" and is an alternative to displacement-controlled loading, in which the displacement is applied at a prescribed rate with respect to time. Force-control loading was the preferred type for this research because it is most representative of loading events on realistic structures.
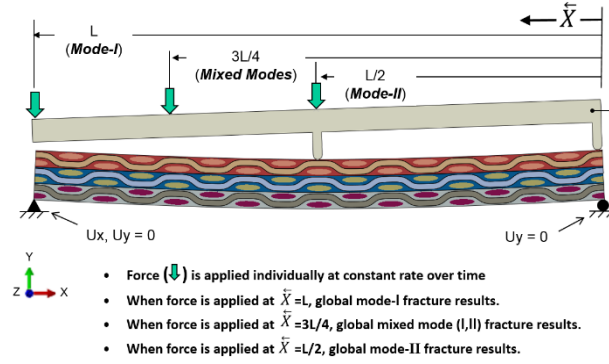
**Figure 3.  Method of Loading and Boundary Conditions for Mixed-Mode Bending Test Simulations of Three-Ply Woven-Fabric Composite Laminate**

Plane stress (2-D) continuum elements of type CPS4 (four-node plane stress element) were used to represent the warp and weft fibers and matrix components.  A plane stress formulation, in contrast to plane strain, was chosen because the model considers the shallow depth of a single warp yarn with respect to the laminate depth (refer to global Z-axis in figure 3). Contact surfaces were defined along the fiber/matrix interfaces for each ply and were assigned tied kinematic restraints.  Note that the initial debond surfaces for the woven composites were not straight lines (or flat planes in 3-D) as those used for unidirectional composites; rather, they were curved surfaces along the central ply's bottom warp (longitudinal) fiber/matrix interface.

No tied contact restraints were assigned to nodes along the initial debond length, as shown in figure 4.  The absence of tied contact restraints at nodes above and below the initial debond regions enabled the unbonded surface region nodes to move independently.  The tied contact restraints ahead of the crack tip were eliminated when the total strain energy release rate $G_{total}$ reached the effective critical strain energy release rate $G_{c\_eff}$.  Once this occurred, strain energy was released and crack growth developed.  Failure was based on LEFM through the use of VCCT.  The VCCT supports crack propagation, but it does not predict crack initiation.  An initial crack must be present.  The mode I and mode II strain energy release rates that determine crack propagation are reported when using VCCT.  Another commonly used modeling approach to fracture analysis of composite laminates is CZM using a traction-separation law (TSL).  The CZM incorporates cohesive surfaces with a TSL that defines a combined strength/damage initiation, damage evolution criteria, and penalty stiffness to model both crack initiation and crack propagation; however, it does not report the individual strain energy release rates.  This research therefore used the VCCT with a representative MMB test specimen and loading.
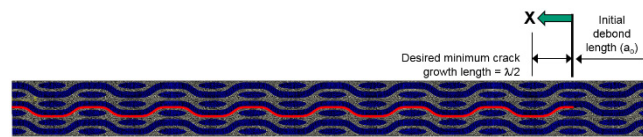


**Figure 4.  Initial Debond Length and Desired Minimum Crack Growth Size**
(Red path represents lower fiber/matrix interface of the central warp fiber
where crack growth is permitted.)

6

Displacement boundary conditions included a pinned support at the laminate's lower left end and roller support at the laminate's lower right end. A rigid loading bar contacted the upper surface of the laminate at the midspan (surface-to-surface contact) and at the right end (tied contact). The effects of geometric nonlinearities from large displacements and contact between the loading bar and the upper surfaces of the laminates were included.

The BK mixed-mode fracture toughness criterion was developed by Benzeggagh and Kenane[3] and is described by equation (1) for 2-D cases. For 3-D cases, the BK criterion includes a mode III strain energy release rate term as shown in equation (2).

$$G_{C\_eff} = G_{IC} + (G_{IIC} - G_{IC}) \left[ \frac{G_{II}}{G_{total}} \right]^{\eta} , \text{ and} \tag{1}$$

$$G_{C\_eff} = G_{IC} + (G_{IIC} - G_{IC}) \left[ \frac{G_{II} + G_{III}}{G_{total}} \right]^{\eta} , \tag{2}$$

where

$G_I$, $G_{II}$, $G_{III}$ are the modes I, II, and III strain energy release rates, respectively,
$G_{IC}$, $G_{IIC}$, $G_{IIIC}$ are the modes I, II, III fracture toughness, respectively,
$G_{total} = G_I + G_{II} + G_{III}$,
$\eta$ is a curve fit parameter that was shown to vary with the matrix ductility,[3]
$G_{C\_eff}$ is the mixed-mode fracture toughness, and
strain energy release rates and fracture toughness terms are expressed in (in.-lb/in.$^2$) units.

The open literature contains minimal data regarding the mode I and mode II critical strain energy release rates for laminated woven composites. The mode I and mode II critical strain energy release rates and material parameter $\eta$ reported by Ranatunga[6] for unidirectional AS4 carbon fiber/3501-6 epoxy laminates were used in this research after the units of measure were converted to the English system of units.


### COMPARISON OF INTERFACIAL FRACTURE BEHAVIORS


Solutions were obtained for each laminate type at each of the three applied force locations ($\check{X} = L$, $\check{X} = 3L/4$, and $\check{X} = L/2$) (see figure 3). Figure 5 shows the effects of loading position on the global $S_{XX}$ stress component for the SB laminate. The applied loads were increased until interfacial crack growth occurred for a minimum of distance of $\lambda/2$. Note that the cleavage deformations shown in the top image of figure 5 correspond to the mode I fracture. The shear-dominated deformations are shown in the inset view for the mode II fracture case.
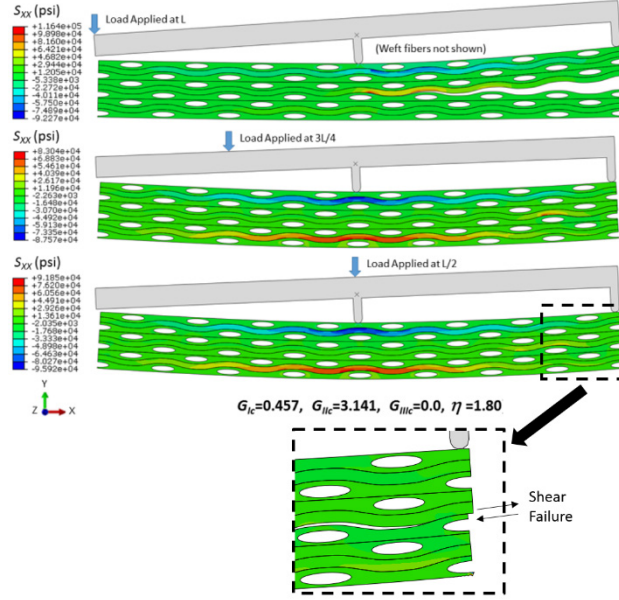
***Figure 5. Contour Plots of $S_{xx}$ for the SB Laminate for Applied Load Locations
at $\overleftarrow{X} = L$, $\overleftarrow{X} = 3L/4$, $\overleftarrow{X} = L/2$***

(Note the extensive crack growth for load applied at $\overleftarrow{X} = L$ (mode I global loading)).

The contour plots in figures 6–8 illustrate the values of $G_{total}/G_{c\_eff}$, $G_I$, and $G_{II}$ for the FB laminate with loading applied at the $\overleftarrow{X} = L$, $\overleftarrow{X}=3L/4$, and $\overleftarrow{X} = L/2$ locations. The strain energy release rates $G_I$, $G_{II}$, $G_{total}$, the $G_{total}/G_{c\_eff}$ ratios, and fracture toughnesses $G_{c\_eff}$ for the FB, SB, and UB laminates were plotted as functions of position along the fiber paths, as shown in figures 9–11. The FB laminate exhibited the greatest variations in strain energy release rates and fracture toughness values along the fiber paths followed by the SB and UB laminates, respectively. Most notable were the regions of zero $G_I$ contributions to the mixed-mode fracture toughness $Gc_{\_eff}$ in the FB and SB laminates occurring for loads applied at the $\overleftarrow{X} = L/2$ (global mode II) and $\overleftarrow{X} = 3L/4$ (global mixed modes I and II) locations. These regions were coincident with large fiber-path angles and experienced localized conversions of $G_I$ to $G_{II}$ strain energy release rates and both $G_{total}$ and $G_{c\_eff}$ increased by nearly 3:1 with respect to their values at the $X = 0$ fiber-path positions.

Reviewing the $G_{c\_eff}$ curves, it can be seen that delaminations will develop earlier in the FB and SB laminates than in the UB laminate; however, the FTCM arrested further crack growth until $G_{total}$ exceeded the higher $G_{c\_eff}$ values resident at the $X = 0.025$ through $X = 0.045$ fiber-path positons.
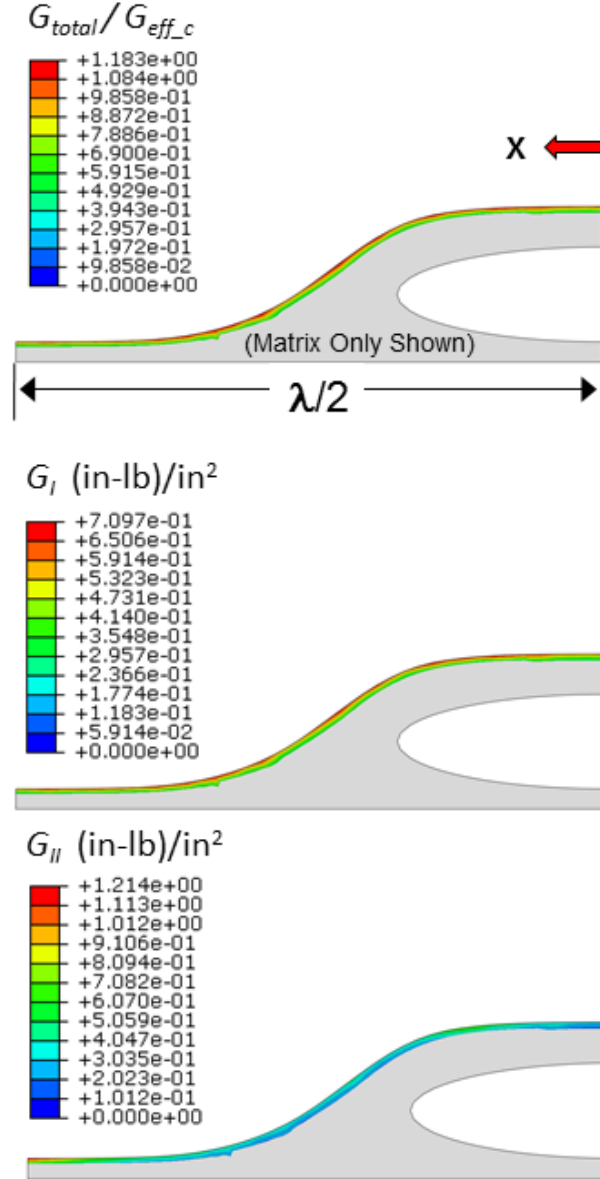
**Figure 6.** **Contour Plots of $G_{total}/G_{c\_eff}$, $G_I$, and $G_{II}$ for the FB Laminate at Warp Fiber/Matrix Interface, Load Applied at $\overleftarrow{X} = L$**
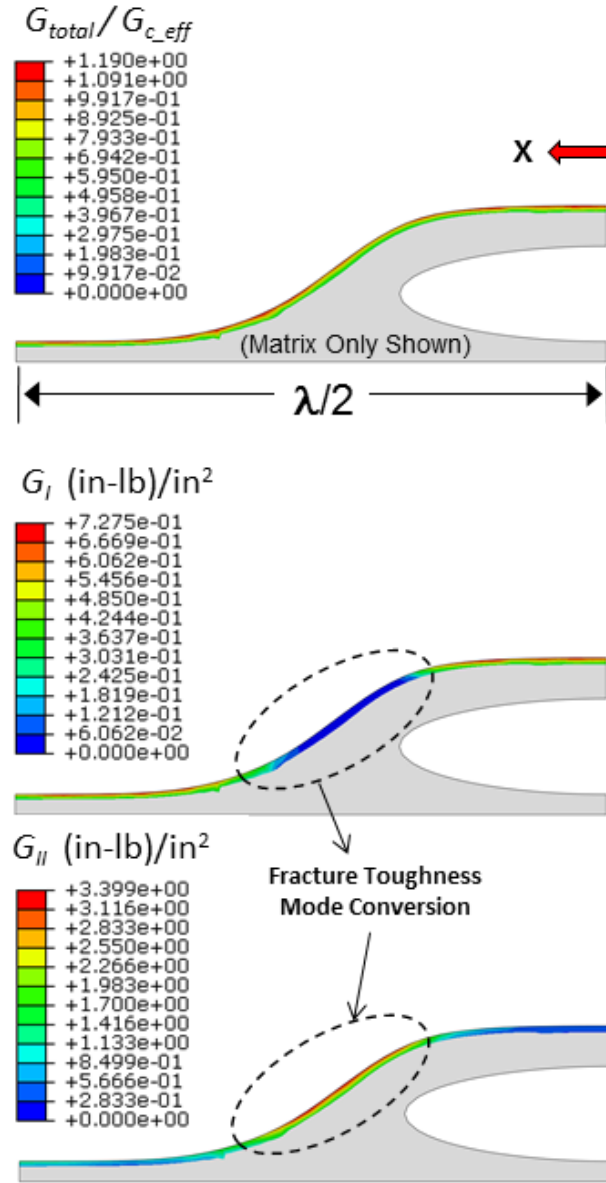
*Figure 7.  Contour Plots of $G_{total}/G_{c\_eff}$, $G_I$, and $G_{II}$ for the FB Laminate at Warp Fiber/Matrix Interface, Load Applied at $\overleftarrow{X} = 3L/4$*
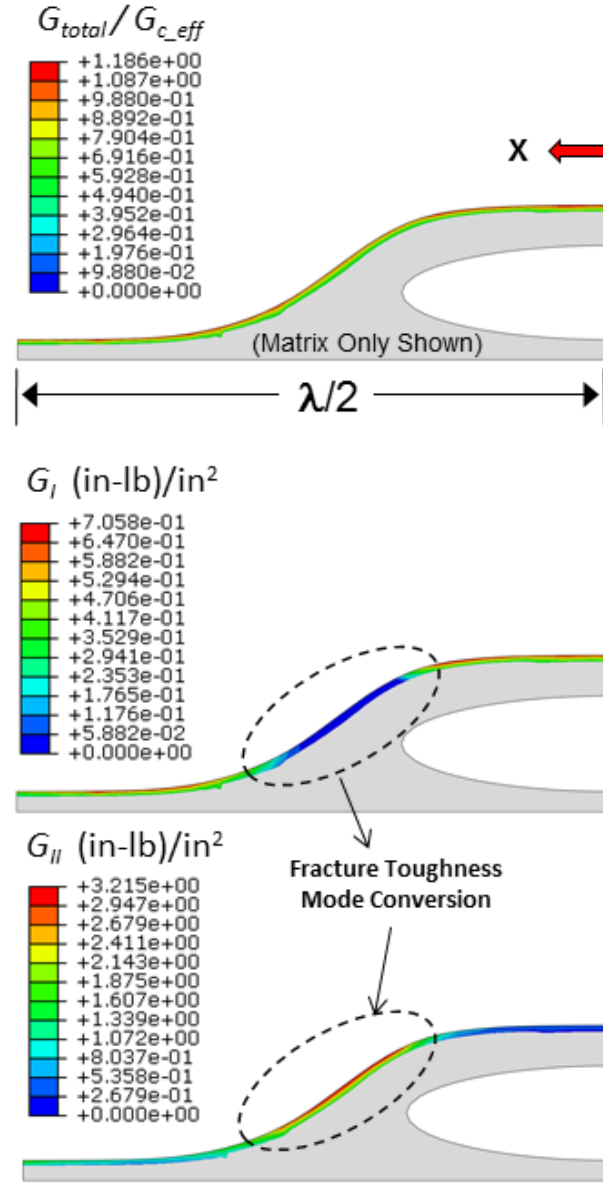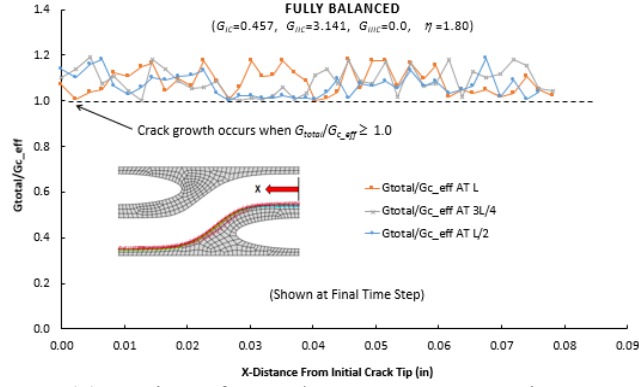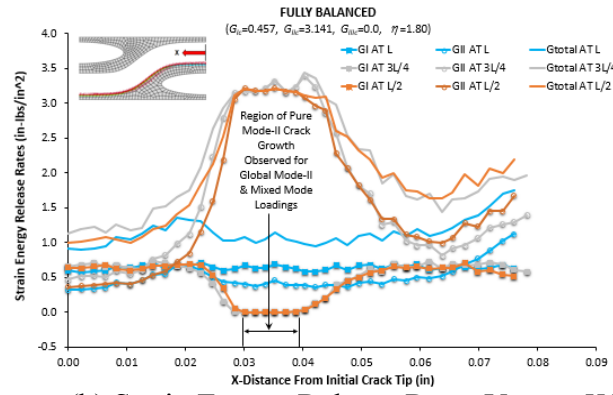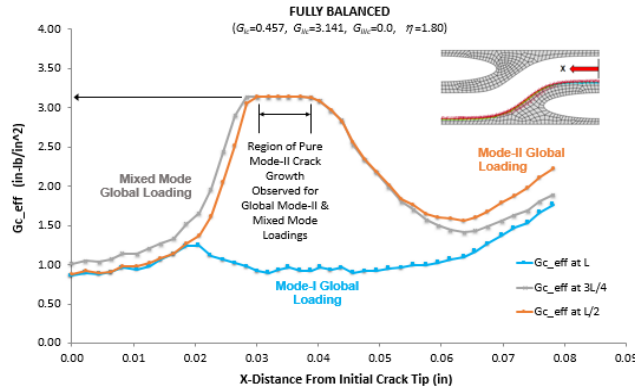
*Figure 8. Contour Plots of $G_{total}/G_{c\_eff}$, $G_I$, and $G_{II}$ for the FB Laminate at Warp Fiber/Matrix Interface, Load Applied at $\overleftarrow{X} = L/2$*

(a) Ratios of $G_{total}/G_{c\_eff}$ Versus *X*-Distance
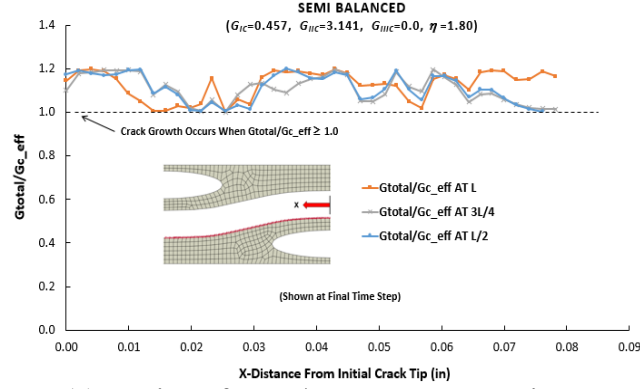


(b) Strain Energy Release Rates Versus *X*-Distance



(c) $G_{c\_eff}$ Versus *X*-Distance

***Figure 9. Plots of $G_{total}/G_{c\_eff}$ Ratio, Strain Energy Release Rates $G_I$, $G_{II}$, $G_{total}$, and Fracture Toughness $G_{c\_eff}$ for the FB Laminate Versus X-Distance from Initial Crack Tip***

12

(a)  Ratios of $G_{total}/G_{c\_eff}$ Versus $X$-Distance



(b) Strain Energy Release Rates Versus $X$-Distance



(c) $G_{c\_eff}$ Versus $X$-Distance

**Figure 10.  Plots of $G_{total}/G_{c\_eff}$ Ratio, Strain Energy Release Rates $G_I$, $G_{II}$, $G_{total}$, and Fracture Toughness $G_{c\_eff}$ for the SB Laminate Versus $X$-Distance from Initial Crack Tip**

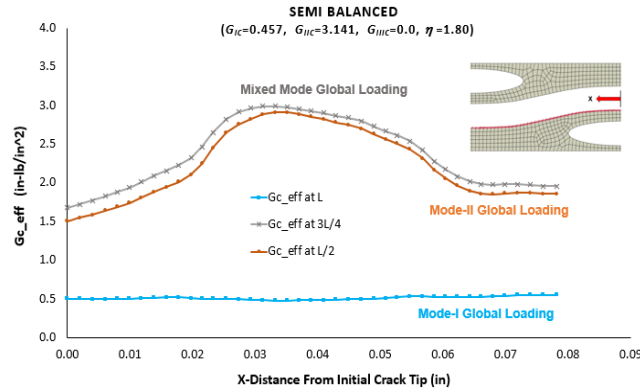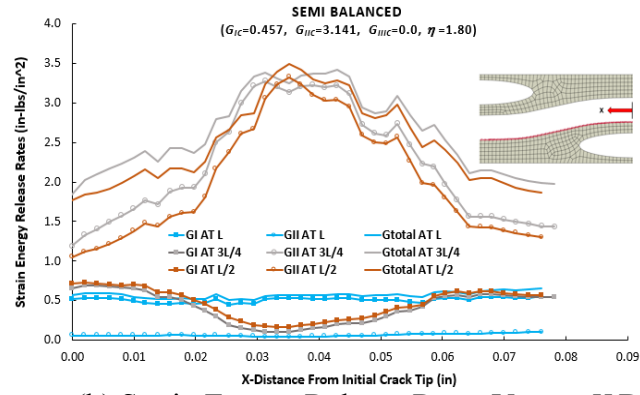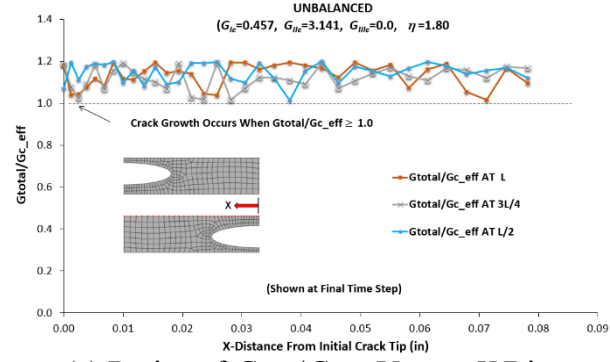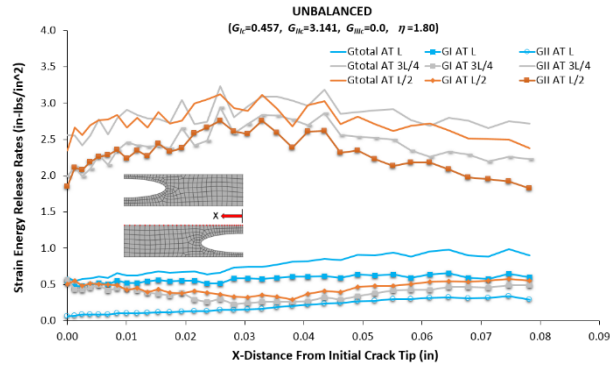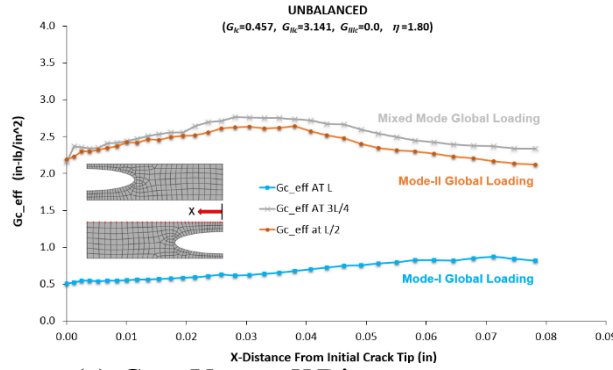(a) Ratios of $G_{total}/G_{c\_eff}$ Versus $X$-Distance



(b) Strain Energy Release Rates Versus $X$-Distance



(c) $G_{c\_eff}$ Versus $X$-Distance

**Figure 11. Plots of Strain Energy Release Rates $G_I$, $G_{II}$, $G_{total}$, and Fracture Toughness $G_{c\_eff}$ for the UB Laminate Versus X-Distance from Initial Crack Tip**

14

Table 3 lists the maximum predicted values of $G_{c\_eff}$ along the fiber paths and the values corresponding to the $X = 0$ fiber path position for each laminate and global loading mode. The $G_{c\_eff}$ values were also plotted in figure 12.

***Table 3. Effective Critical Strain Energy Release Rates, $G_{c\_eff}$ for $0 \leq x \leq \lambda/2$***

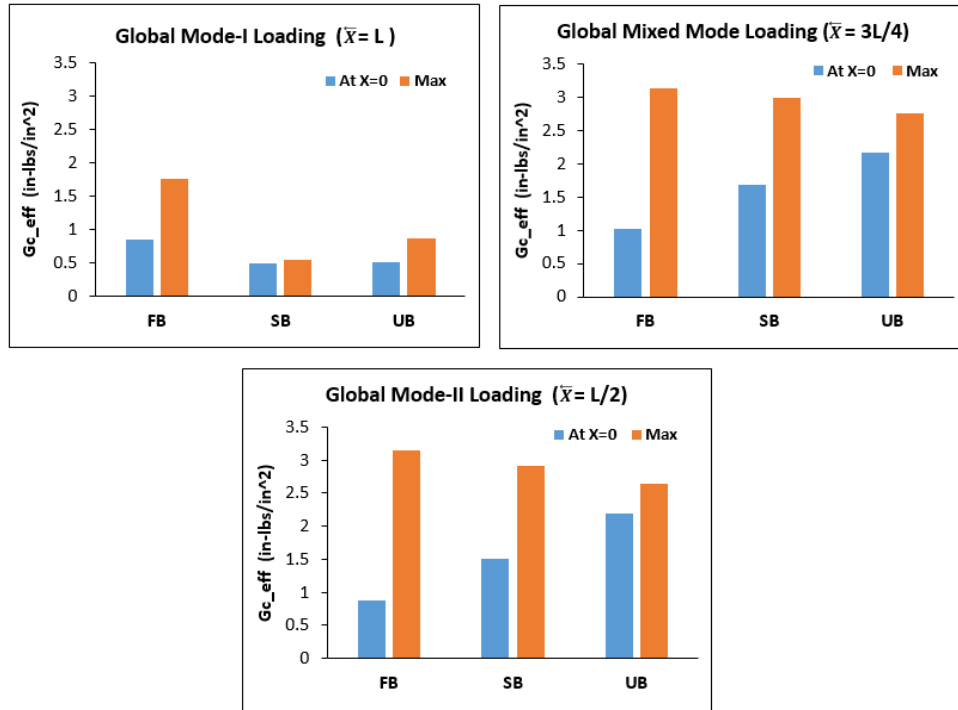| Global Loading Mode | Laminate Type | $G_{c\_eff}$ at X = 0 (in.-lb)/in.$^2$ | Maximum $G_{c\_eff}$ (in.-lb)/in.$^2$ |
|---|---|---|---|
| I | FB | 0.859 | 1.770 |
| | SB | 0.501 | 0.555 |
| | UB | 0.505 | 0.870 |
| II | FB | 0.881 | 3.141 |
| | SB | 1.505 | 2.907 |
| | UB | 2.190 | 2.640 |
| Mixed Modes(I, II ) | FB | 1.020 | 3.141 |
| | SB | 1.680 | 2.990 |
| | UB | 2.160 | 2.760 |



***Figure 12. Plots of the Effective Critical Strain Energy Release Rates, $G_{c\_eff}$ Versus Laminate and Global Loading Type***

The observed strain energy release rate conversion mechanism was further investigated by examination of the stress components along the fiber paths. A stress transformation was performed using equation (3) to resolve the global coordinate system to a local coordinate system. The local system provided the interlaminar tangential, normal, and shear stress components $S_{LX}$, $S_{LY}$, and $S_{LXY}$, respectively, along the fiber/matrix interfaces. Figures 13–15 show the global and interlaminar stress components at the immediate time step preceding crack growth. Note that the global and local coordinate systems for the UB laminate model were identical; therefore, the interlaminar stresses were equal to the global stress components. Interfacial delaminations will initiate when the interlaminar normal stress $S_{LY}$ is tensile in sense and/or the interlaminar shear stress $S_{LXY}$ exceed their respective interface strength levels.

$$\begin{Bmatrix} S_{LX} \\ S_{LY} \\ S_{LXY} \end{Bmatrix} = \begin{bmatrix} cos^2\theta & sin^2\theta & -2cos\theta sin\theta \\ sin^2\theta & cos^2\theta & 2cos\theta sin\theta \\ cos\theta sin\theta & -cos\theta sin\theta & cos^2\theta - sin^2\theta \end{bmatrix} \begin{Bmatrix} S_X \\ S_{YY} \\ S_{XY} \end{Bmatrix}, \tag{3}$$

where $\theta$ is measured from the tangent vector along the fiber path to the global x-axis and is expressed in radians, and $S_X$, $S_Y$, $S_{XY}$, $S_{LX}$, $S_{LY}$, and $S_{LXY}$ are expressed in units of psi.
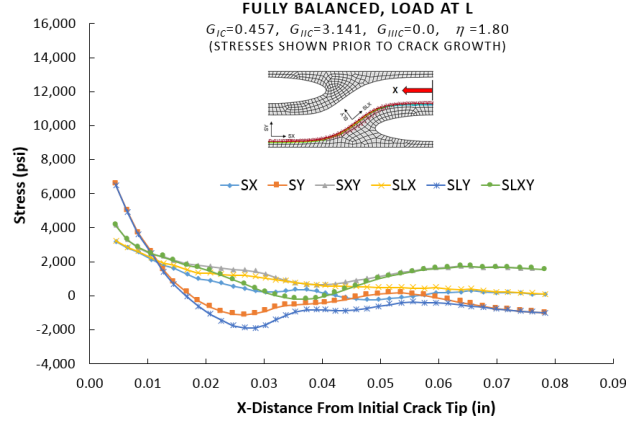
(a) Load Applied at $\overleftarrow{X} = L$
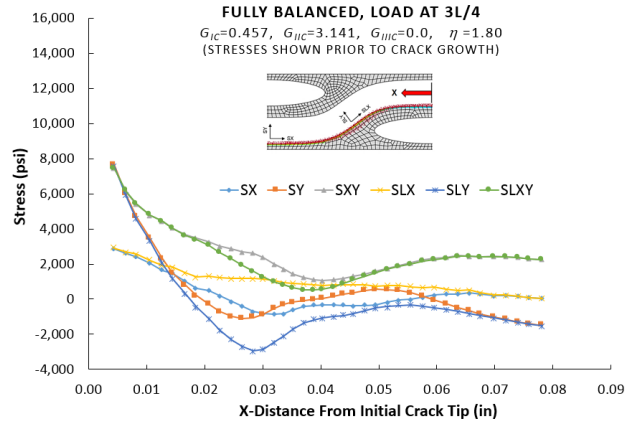

(b) Load Applied at $\overleftarrow{X} = 3L/4$
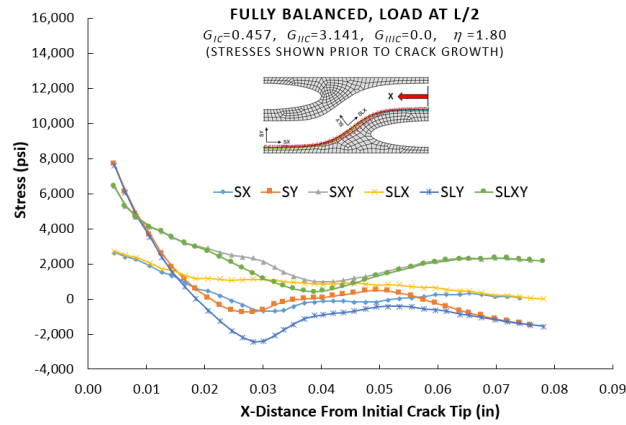

(c) Load Applied at $\overleftarrow{X} = L/2$

*Figure 13.  Plots of Global and Local Stress Components Versus X-Distance from Initial Crack Tip Shown Immediately Preceding Crack Growth for the FB Laminate*

17
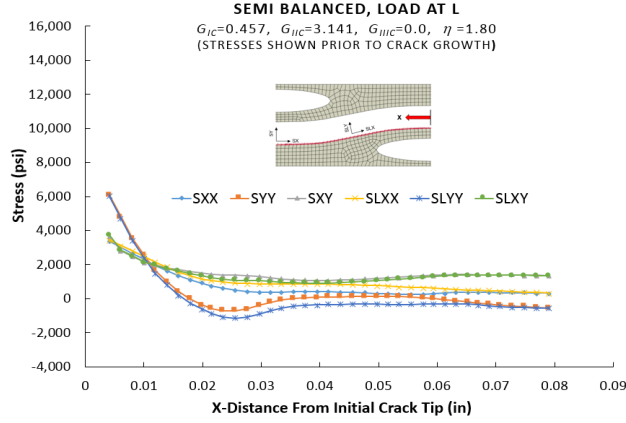
(a) Load Applied at $\overleftarrow{X} = L$



(b) Load Applied at $\overleftarrow{X} = 3L/4$



(c) Load Applied at $\overleftarrow{X} = L/2$

*Figure 14. Plots of Global and Local Stress Components Versus X-Distance from Initial Crack Tip Shown Immediately Preceding Crack Growth for the SB Laminate*

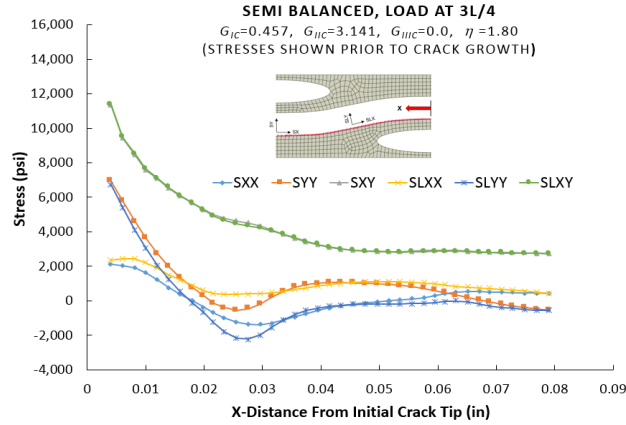(a) Load Applied at $\overleftarrow{X} = L$



(b) Load Applied at $\overleftarrow{X} = 3L/4$
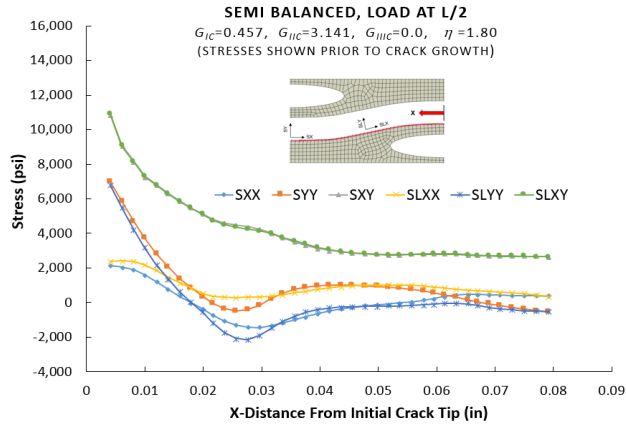


(c) Load Applied at $\overleftarrow{X} = L/2$

***Figure 15.  Plots of Global Stress Components Versus X-Distance from Initial Crack Tip***
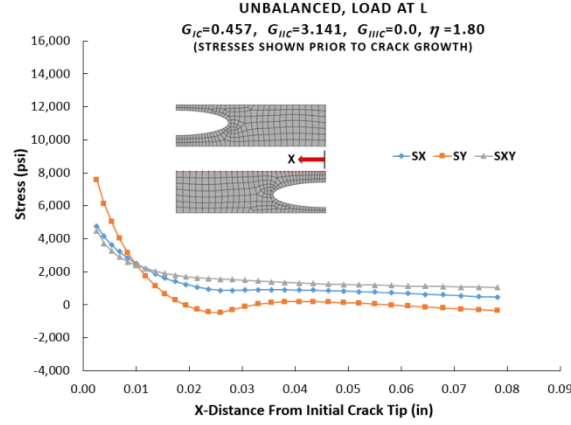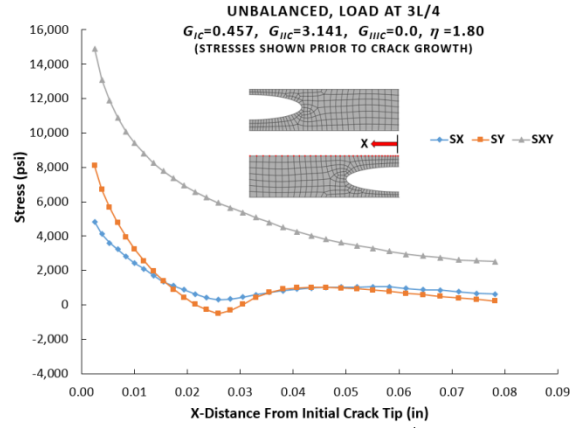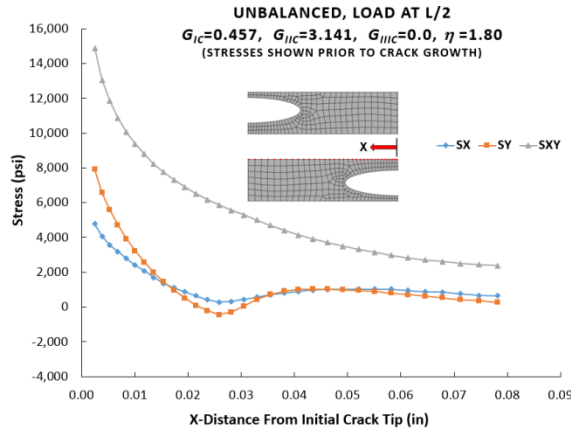***Shown Immediately Preceding Crack Growth for the UB laminate***
(Note that the global and local stress components were the same for the UB laminate.)

The applied loads immediately prior to crack growth and the peak local stresses in the vicinity of the initial crack tip (at $X = 0.004$ inch) immediately prior to crack growth are listed in table 4. The loads were observed to increase from the mode I to mode II to the mixed-mode case as expected because of the differences in the $G_{Ic}$ and $G_{IIc}$ values used. In a similar fashion, the loads were also observed to increase with laminate type in increasing order from the FB laminate to the SB laminate to the UB laminate. Recall, however, that the laminate thickness for each type increases accordingly as shown in table 2. The normal and shear stress components generally dominated the three types of global loadings. (Note that the local and global coordinate systems were identical for the UB laminate and, as such, the corresponding stress values in table 4 were simply designated using the local stress nomenclature.) The shear strain energies served to increase $G_{c\_eff}$ for the FB and SB laminates when they were subjected to mixed-mode and mode II global loadings. This phenomenon was also observed by Shindo.[4] The local tangential stress components $S_{LX}$ were the smallest values for the mode II and mixed-mode loadings across each laminate style. The maximum interface stresses achieved just prior to crack growth were generally observed for the UB laminate for each of the three loading modes. For this laminate and the mode II and mixed-mode loadings, the shear stresses were the maximum components developed, followed by the normal and tangential components, respectively. The maximum shear stresses achieved for the mixed mode ($\bar{X} = 3L/4$) and mode II ($\bar{X} = L/2$) loadings of the UB laminate were nearly identical as the mode I strain energies developed in the mixed mode case had minimal influence on the stress distributions near the crack front.

The stress components in table 4 are especially useful for defining TSLs for modeling woven composite laminates with CZMs; however, it is important that the TSLs are defined using the local stress components and strain energy release rates to ensure proper calculations of interfacial delaminations.

***Table 4.  Applied Loads and Peak Local Stress Components***
***(Near Crack Tip at X = 0.004 inch) Prior to Crack Growth***

**FB Laminate**

|  | | **Mode I** | **Mode II** | **Mixed Modes** |
|---|---|---|---|---|
| Load | (lb) | 53.46 | 129.00 | 204.60 |
| $S_{LX}$ | (psi) | 3223.92 | 2717.98 | 2916.93 |
| $S_{LY}$ | (psi) | 6484.23 | 7618.80 | 7600.95 |
| $S_{LXY}$ | (psi) | 4124.33 | 6425.04 | 7478.75 |

**SB Laminate**

|  | | **Mode I** | **Mode II** | **Mixed Modes** |
|---|---|---|---|---|
| Load | (lb) | 62.75 | 233.6 | 381.5 |
| $S_{LX}$ | (psi) | 3438.53 | 2,359.75 | 2124.83 |
| $S_{LY}$ | (psi) | 6003.55 | 6789.23 | 6716.27 |
| $S_{LXY}$ | (psi) | 3718.03 | 10898.10 | 11384.30 |

**UB Laminate**

|  | | **Mode I** | **Mode II** | **Mixed Modes** |
|---|---|---|---|---|
| Load | (lb) | 78.52 | 325.10 | 467.00 |
| $S_{LX}$ | (psi) | 4770.03 | 4775.18 | 4842.57 |
| $S_{LY}$ | (psi) | 7586.65 | 7915.91 | 8103.26 |
| $S_{LXY}$ | (psi) | 4486.59 | 14890.40 | 14917.10 |

The VCCT also reports the nodal debond times (DBTs) corresponding to the nodes along the slave cohesive surfaces.  Crack growth stability was examined by plotting DBT for each laminate and loading type versus position along the fiber paths as shown in figure 16.  Unstable crack growth occurred when the slopes of the DBT versus position approach zero.  The FB laminate demonstrated the highest levels of crack growth stability followed by the SB and UB laminates, respectively; however, the FB and SB laminates showed varying levels of crack growth stability that were dependent on position along the crimped fiber paths.  The highest crack growth stability levels for these two laminates were observed near regions of maximum change in slope along the fiber paths (approximately 0.025 inch); however, crack growth became completely unstable once crack lengths exceeded 0.040 inch.  The UB laminate, which initially exhibited stable crack growth up to a crack length equal to 1.2e-03 inches became completely unstable at larger crack lengths.
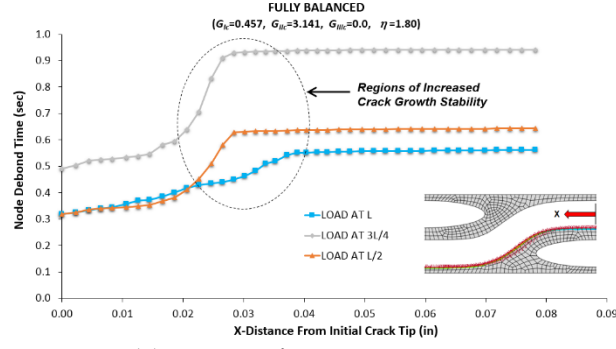
(a) FB Laminate
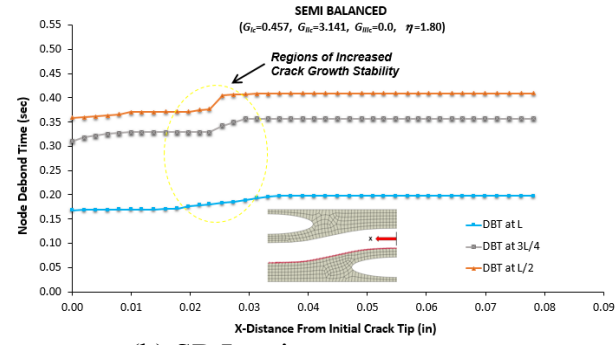

(b) SB Laminate
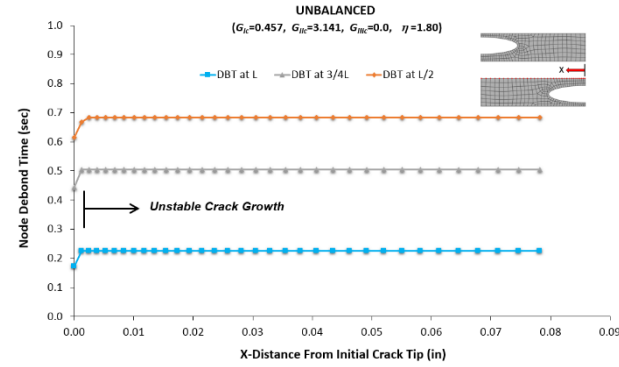

(c) UB Laminate

*Figure 16.  Plots of Nodal Debond Times for the FB (a), SB (b), and UB (c) Laminates Versus X-Distance from Initial Crack Tip*

22

## SUMMARY AND CONCLUSIONS

Numerical models were conducted at the mesoscale for three variations of a plain-woven fabric composite subjected to mode I, mode II, and mixed-mode global loadings. The effects of crimped fiber paths on the effective critical strain energy release rates were investigated using the virtual crack closure technique with the Benzeggagh-Kenane mixed-mode fracture criterion. Results demonstrated there were considerable effects for the FB and SB laminates when they were subjected to mixed-mode and mode II global loadings. Increasing contributions from the localized mode II strain energy release rates along the crimped fiber paths served to increase the mixed-mode fracture toughness $G_{c\_eff}$, as also reported by Shindo.[4]

In addition to the fiber bridging, the observed fracture toughness conversion mechanism resulting from the curvilinear fiber paths with $G_{IIc} > G_{Ic}$ provides further insight into how woven composites exhibit greater damage tolerance thresholds than do unidirectional composites. Under force-control loading, the FB laminate exhibited the highest crack growth stability, followed by the SB and UB laminates; however, the UB laminate in general supported the highest stresses near the vicinity of the initial debond region prior to crack propagation, provided virtually no crack growth stability.

Results of this investigation demonstrate that increased delamination resistance and crack growth stability can be achieved through careful selection of the woven fabric architectures by further consideration of the mixed-mode fracture behaviors at the fiber/matrix interfaces.

Future studies will conduct experiments to provide measured properties for candidate fiber materials as their constitutive behaviors are expected to be transversely isotropic.

## REFERENCES

1.  Edmund F. Rybicki and Melvin F. Kanninen, "A Finite Element Calculation of Stress Intensity Factors by a Modified Crack Closure Integral," *Engineering Fracture Mechanics*, vol. 9, no. 4, pp. 931–938, 1977.

2.  Ronald Krueger, "The Virtual Crack Closure Technique: History, Approach and Applications," NASA/CR-2002-211628, ICASE Report No. 2002-10, ICASE, National Aeronautics and Space Administration, Langley Research Center, Hampton, VA, April 2002.

3.  M. L. Benzeggagh and M. Kenane, "Measurement of Mixed-Mode Delamination Fracture Toughness of Unidirectional Glass/Epoxy Composites with Mixed-Mode Bending Apparatus," *Composites Science and Technology*, vol. 56, no. 4, pp. 439–449, 1996.

4. Y. Shindo, S. Takahashi, T. Takeda, F. Narita, S. Watanabe, "Mixed-Mode Interlaminar Fracture and Damage Characterization in Woven Fabric-Reinforced Glass/Epoxy Composite Laminates at Cryogenic Temperatures using the Finite Element and Improved Test Methods," *Engineering Fracture Mechanics*, vol. 75, no. 18, pp. 5101–5112, 2008.

5. American Society for Testing and Materials, "Standard Test Method for Mixed Mode I-Mode II Interlaminar Fracture Toughness of Unidirectional Fiber Reinforced Polymer Matrix Composites," ASTM-D-6671-06, ASTM International, West Conshohocken, PA.

6. V. Ranatunga, "Finite Element Modeling of Delamination Crack Propagation in Laminated Composites," *Proceedings of the World Congress on Engineering 2011*, vol. III, WCE 2011, London, United Kingdom, July 6–8, 2011.

7. P. P. Camanho and C. G. Dávila, "Mixed-Mode Decohesion Finite Elements for the Simulation of Delamination in Composite Materials," NASA/TM-2002-211737, National Aeronautics and Space Administration, Langley Research Center, Hampton, VA, June 2002.

8. D. Motamedi, A. S. Milani, "Mixed-Mode Fracture Analysis of Delamination Using Non-Linear Extended Finite Element Method," submitted to *The 19$^{th}$ International Conference on Composite Materials*, Paris, France, January 23–24, 2017.

9. Andrew W. Hulton and Paul V. Cavallaro, "Comparing Computational and Experimental Failure of Composites Using XFEM," *Proceedings of the ASME 2016 International Mechanical Engineering Congress & Exposition*, IMECE2016-65232, Phoenix, AZ, November 11–17, 2016.

10. D. A. Hawkins, Jr., A. Haque, "Strain Energy Release Rate and Mode-I Delamination Growth in Carbon-Graphene/Epoxy Hybrid Nanocomposites," *6$^{th}$ BSME International Conference on Thermal Imaging (ICTE 2014), Proceedia Engineering*, vol. 105, pp. 829–834, 2015.

11. Paul V. Cavallaro, "Effects of Weave Styles and Crimp Gradients on Woven Kevlar Epoxy Composites," *Experimental Mechanics*, vol. 56, no. 4, pp. 617–635, 2016.

12. ABAQUS, Ver. 6.10, Dassault Systèmes, Waltham, MA.

13. J. R. Reeder, "An Evaluation for Mixed-Mode Delamination Behavior Criteria," NASA Technical Memorandum 104210, National Aeronautics and Space Administration, Langley Research Center, Hampton, VA, February 1992.

## INITIAL DISTRIBUTION LIST

| Addressee | No. of Copies |
|---|---|
| U.S. Army Research Laboratory, Aberdeen Proving Ground, MD (AMSRD-ARL-WM-MD (B. Cheeseman, C. Yan, B. Scott), RDRL-WMM-D (V. Champagne, Jr.), RDRL-WMP-F (A. Frydman), RDRL-WMM-A (M. Maher)) | 6 |
| U.S. Army Aberdeen Test Center, Aberdeen Proving Ground, MD (TEDT-AT-WFT (F. Carlen)) | 1 |
| U.S. Army Natick Soldier Research, Development, and Engineering Center, Natick, MA (R. Benney, P. Blanas, P. Cunniff, K. Horak, M. Jee, J. Mackiewicz, M. Maffeo, G. Proulx, C. Quigley, R. Sykes, G. Thibault, S. Tucker, J. Ward) | 13 |
| U.S. Army Research Office (RDRL-RO-EN (D. Stepp, W. Mullins)) | 2 |
| Navy Clothing and Textile Research Facility, Natick, MA (B. Avellini, L. Caulfield, T. Hart, C. Heath) | 4 |
| Naval Surface Warfare Center, Panama City, FL (Code CX05 (F. Garcia)) | 1 |
| Naval Surface Warfare Center, Carderock Division, W. Bethesda, MD (P. Dudt, R. Crane, E. Rasmussen) | 3 |
| Naval Surface Warfare Center, Dahlgren Division, Dahlgren, VA (S. Bartyczak, W. Mock) | 2 |
| Office of Naval Research, Arlington, VA (ONR-331 (R. Barsoum), ONR-DOI (L. Schuette), ONR-334 (Y. Rajapakse)) | 3 |
| Defense Technical Information Center | 1 |
| Center for Naval Analyses | 1 |
| University of Rhode Island, Kingston, RI (A. Shukla) | 1 |
| City College of the City University of New York, NY (A. Sadegh) | 1 |
| University of British Columbia, Kelowna, BC, Canada (A. Milani) | 1 |
| JPS Composite Materials, Anderson SC (M. Salama) | 1 |
| Core Composites, Bristol, RI (R. O'Meara) | 1 |
| Warwick Mills, New Ipswich, NH (C. Howland) | 1 |